International Journal of
Environmental Research and Public Health

MDPI

Article

Two-Dimensional Titanium Carbides ($Ti_3C_2T_x$) Functionalized by Poly(m-phenylenediamine) for Efficient Adsorption and Reduction of Hexavalent Chromium

Linfeng Jin [1], Liyuan Chai [1,2,3], Weichun Yang [1,2,3], Haiying Wang [1,2,3,*] and Liyuan Zhang [4,*]

1 School of Metallurgy and Environment, Central South University, Changsha 410083, China; jlfcsu@163.com (L.J.); chailiyuan@csu.edu.cn (L.C.); yang220@csu.edu.cn (W.Y.)
2 Chinese National Engineering Research Center for Control and Treatment of Heavy Metal Pollution, Changsha 410083, China
3 Water Pollution Control Technology Key Lab of Hunan Province, Changsha 410004, China
4 Department of Colloid Chemistry, Max Planck Institute of Colloids and Interfaces, 14476 Potsdam, Germany
* Correspondence: haiyw25@yahoo.com (H.W.); zhang_livyl@csu.edu.cn (L.Z.); Tel.: +86-731-8883-0875 (H.W.); Fax: +86-731-8871-0171 (H.W.)

Received: 30 November 2019; Accepted: 20 December 2019; Published: 25 December 2019

Abstract: Titanium carbides (MXenes) are promising multifunctional materials. However, the negative surface charge and layer-by-layer restacking of MXenes severely restrict their application in the field of anionic pollutants, including in hexavalent chromium (Cr(VI)). Herein, $Ti_3C_2T_x$ MXenes was functionalized through in situ polymerization and intercalation of poly(m-phenylenediamine) (PmPD), then $Ti_3C_2T_x$/PmPD composites were obtained. Delightedly, $Ti_3C_2T_x$/PmPD composites exhibited positive surface charge, expanded interlayer spacing, and enhanced hydrophobicity. Furthermore, the specific surface area of $Ti_3C_2T_x$/PmPD composite was five and 23 times that of $Ti_3C_2T_x$ and PmPD, respectively. These advantages endowed $Ti_3C_2T_x$/PmPD composite with an excellent adsorption capacity of Cr(VI) (540.47 mg g^{-1}), which was superior to PmPD (384.73 mg g^{-1}), $Ti_3C_2T_x$ MXene (137.45 mg g^{-1}), and the reported MXene-based adsorbents. The Cr(VI) removal mechanism mainly involved electrostatic adsorption, reduction, and chelation interaction. This study developed a simple functionalization strategy, which would greatly explore the potential of MXenes in the field of anionic pollutants.

Keywords: titanium carbides; functionalization; polymerization; hexavalent chromium; adsorption

1. Introduction

Hexavalent chromium (Cr(VI)) pollution poses a serious crisis to human beings and the ecosystem, due to its high mobility, toxicity, and potential carcinogenicity [1,2]. It is extremely urgent to treat Cr(VI) contamination. In contrast, trivalent chromium (Cr(III)) usually has low levels of toxicity, is immobile, and even is an essential micronutrient for organisms [3–5]. At present, adsorption remains an effective method for Cr(VI) remediation [6], which involves the conversion from toxic Cr(VI) to mild Cr(III) in the adsorption process [7,8]. Various adsorbents have been developed, such as biochar [9,10], the metal–organic framework [11,12], nanoscale zero-valent iron [13,14], graphene oxide [15,16], and organic polymer [17,18]. Unfortunately, current adsorbents generally suffer from unsatisfactory removal capacity, a low adsorption rate, and weak reduction capacity. Therefore, the development of novel adsorbents with an outstanding performance is still a paramount challenge.

Transition metal carbides (MXenes) are novel two-dimensional (2D) materials, which were first reported by Yury Gogotsi in 2011 [19–21]. Their unique physicochemical properties (such as a

layered structure, high hydrophilic surface, and excellent electrical conductivity) endow MXenes with promising advantages in electromagnetic interference shielding [22], energy storage fields [23], and conducting thin films [24]. In recent years, MXenes have received increasing attention in the field of environment owning to their large amounts of surface negative terminations (such as -O, -OH, and -F) [25–27]. These negative terminations render MXenes with favorable removal capacity for cationic pollutants.

However, MXenes still face great challenges in the remediation of anionic pollutants due to the charge repulsion between MXenes and anionic pollutants [28]. Moreover, due to the hydrogen bonding between the surface functional groups, MXenes are always reassembled as tightly as graphene and other 2D materials in practical applications [29,30], which would inevitably decrease the mass transfer efficiency and availability of MXenes [31]. Regulating surface charge and interlayer spacing are feasible approaches to fully explore the potential of MXenes in the field of Cr(VI) remediation. However, there is still no relevant report on this at present.

As a kind of conjugated polymer, poly(m-phenylenediamine) (PmPD) has been widely employed to functionalize matrix materials because of its simple synthesis and abundant amino groups [32–34]. In this research, $Ti_3C_2T_x$ (X = OH, O or F) was selected as the representative of the MXenes family, and the regulation of surface charge and expansion of interlayer spacing of $Ti_3C_2T_x$ were successfully achieved by in situ polymerization and intercalation of PmPD. Accordingly, a novel MXenes/poly(m-phenylenediamine) ($Ti_3C_2T_x$/PmPD) composite was obtained and utilized to adsorb Cr(VI) from aqueous solution. Finally, the preparation mechanism and adsorption mechanism were investigated in detail.

2. Material and Methods

2.1. Materials

Ti_3AlC_2 MAX powder (400 mesh) was purchased from 11 Technology Co., Ltd. m-Phenylenediamine (99.5%) was purchased from Aladdin Reagent. All other reagents were of an analytical grade and were purchased from Sinopharm Chemical Reagent.

2.2. Preparation of $Ti_3C_2T_x$, $Ti_3C_2T_x$/PmPD, PmPD

$Ti_3C_2T_x$ was synthesized by etching and delaminating Ti_3AlC_2 MAX powder through the typical minimally intensive layer delamination (MILD) approach [20]. $Ti_3C_2T_x$ solution with different concentrations was obtained by dissolving $Ti_3C_2T_x$ in deionized (DI) water. The detail process of $Ti_3C_2T_x$ synthesis was described in the supporting information.

To synthesis $Ti_3C_2T_x$/PmPD, 1 g mPD monomer was firstly dissolved in 30 mL DI water, and added to a certain concentration of 100 mL $Ti_3C_2T_x$ dispersion. The above mixture was continuously sonicated and stirred for 30 minutes. After that, $Na_2S_2O_8$ solution (20 mL, 0.11 g mL^{-1}) was slowly added to the above solution, and the reaction was maintained for 4 h, at −4 °C by ice bath. $Ti_3C_2T_x$/PmPD composites with different mass ratios of mPD to $Ti_3C_2T_x$ were prepared in turn by changing the concentration of $Ti_3C_2T_x$. The obtained composites were labeled $Ti_3C_2T_x$/PmPD-X (mass ratios X = 2/1, 5/1, 10/1). The final sediment was centrifuged, rinsed with amount DI water, and dried under vacuum (−55 °C, 12 h). Finally, $Ti_3C_2T_x$/PmPD-X composites were obtained.

2.3. Characterization

The morphology and structure of as-obtained composites were characterized by scanning electron microscope (SEM, FEI Nova NanoSEM 230, FEI company, Hillsboro, OR, USA), scanning transmission electron microscope (STEM-EDS, JEM-2100F, Japan Electronics Co., Ltd. (JEOL), Tokyo, Japan), atomic force microscope (AFM, NanoMan VS, Bruker, Germany), X-ray powder diffraction patterns (XRD, D/max 2550 VB + XX diffractometer, Rigaku International Corp, Tokyo, Japan), X-ray photoelectron spectroscopy (XPS, K-Alpha 1063, Thermo Scientific, Waltham, MA, USA), Raman scattering spectra

(532 nm, Renishaw inVia, Renishaw, London, England), and Fourier transformed infrared spectra (FT-IR, Nicolet IS10, Thermo Scientific, Waltham, MA, USA). The contact angles were measured using a Date Physics JY-82C goniometer (Dingsheng testing machine testing equipment Co., Ltd, Jinan, China). Zeta potentials were recorded using a Malvern Nano-ZS Zetasizer. The N_2 adsorption-deposition isotherms were measured by bjbuilder KUBO-X1000 (Beijing Builder Electronic Technology Co., Ltd., Beijing, China).

2.4. Batch Experiments

Potassium dichromate ($K_2Cr_2O_7$) was dissolved in DI water to obtain aqueous solutions with different Cr (VI) concentrations. The obtained composites (10 mg) were put into 100 mL polyethylene bottle with 20 mL Cr(VI) solution, then the mixture was shaken at 30 °C for 12 h at 180 rpm speed. UV−vis spectrophotometer (540 nm) was utilized to detect the residual Cr(VI) concentration. All the experimental data were the average values of three measurements, whose relative error was less than 5%.

3. Results and Discussion

3.1. Material Characterization

The structure and morphology of as-obtained composites were studied by using TEM, SEM, XRD, AFM, and XPS technologies. As can be seen from Figure 1a–c, $Ti_3C_2T_x$ MXene exhibited 2D ultrathin morphology with a small average thickness of ~4 nm. The disappearance of the peak at 39° and the shift of the (002) peak to 6.04° also indicated the formation of $Ti_3C_2T_x$ nanosheets (Figure 1d) [35,36]. As shown in Figure 1e–g, $Ti_3C_2T_x$/PmPD-X composites showed a 2D dispersed and wrinkled morphology with a thickness ranging from ~15 nm to ~70 nm. In addition, taking $Ti_3C_2T_x$/PmPD-5/1 as an example, $Ti_3C_2T_x$/PmPD-X composites owned a thin and uniform shape (Figure 1i). The homogeneous dispersion of C, Ti, and N elements also revealed the homogeneous polymerization of PmPD on surface $Ti_3C_2T_x$ nanosheets (Figure 1j).

As can be seen from Figure 1d, the (002) peak of $Ti_3C_2T_x$/PmPD-2/1 shifted to a smaller 2θ angle (5.54°) compared to that of $Ti_3C_2T_x$ (6.04°). The decreased 2θ angle indicated a significant expansion of the interlayer spacing of $Ti_3C_2T_x$/PmPD-2/1 from 14.6 to 15.9 Å. Furthermore, the (002) peak of $Ti_3C_2T_x$/PmPD-5/1 shifted to 5.02° (17.6 Å interlayer spacing), which increased about 3.0 Å compared to that of original $Ti_3C_2T_x$. In addition, with the further increase of mass ratio of mPD to $Ti_3C_2T_x$, the (002) peak of $Ti_3C_2T_x$/PmPD-10/1 would shift to the minimum 2θ angle, revealing that the interlayer spacing of $Ti_3C_2T_x$ nanosheets were further expanded. The enlargement of interlayer spacing may be ascribed to the intercalation of PmPD in the polymerization process as well as the barrier effect of PmPD layer. These results revealed that the interlayer spacing of PmPD/$Ti_3C_2T_x$ composites could be regulated from 14.6 to 17.6 Å, or even greater, by adjusting the mass ratio. It was noteworthy that the expansion of interlayer spacing would facilitate exposing the active sites and developing the adsorption potential of $Ti_3C_2T_x$ MXene.

XPS spectrum were shown in Figure 1h. The presence of N element on intermediate $Ti_3C_2T_x$/mPD indicated that mPD monomers were enriched on the $Ti_3C_2T_x$ surface through electrostatic interaction and hydrogen bonding [37]. The enrichment of mPD was beneficial to the uniform polymerization of PmPD. The peak of N element was gradually enhanced with the increase of mass ratio of mPD to $Ti_3C_2T_x$, which corresponded to the increase of composites thickness. In contrast, pure PmPD was homogeneously polymerized in solution and formed spherical shape with a diameter of 200–2000 nm (Figure S1). In contrast, no spherical morphology was observed in $Ti_3C_2T_x$/PmPD composites, which further indicated the uniform polymerization of mPD on $Ti_3C_2T_x$ surface.

In the contact angle experiments (Figure 1k right), the water droplet was immediately absorbed by $Ti_3C_2T_x$ within ~1 s, which indicated that $Ti_3C_2T_x$ had high hydrophilicity. It is commonly known that high hydrophilicity of $Ti_3C_2T_x$ provides a good dispersion, which makes the adsorbent difficult

to separate after treating pollutants [38]. In contrast, the contact angle of $Ti_3C_2T_x$/PmPD increased to ~59° (Figure 1k left), which meant that the hydrophobicity of $Ti_3C_2T_x$/PmPD was improved. The improvement of hydrophobicity was helpful to enhance the separation and recycling ability of $Ti_3C_2T_x$/PmPD. N_2 adsorption-desorption isotherms and calculated parameters were displayed in Figure 1l and Table 1, respectively. The specific surface areas of $Ti_3C_2T_x$ and PmPD were 10.42 and 2.44 m^2 g^{-1}, respectively. The unfavorable specific surface area was probably caused by serious restacking [30]. Nevertheless, the specific surface areas of $Ti_3C_2T_x$/PmPD-X were far beyond that of $Ti_3C_2T_x$ and PmPD. In addition, the specific surface area of $Ti_3C_2T_x$/PmPD-5/1 was five and 23 times that of $Ti_3C_2T_x$ and PmPD, respectively. The improvement of specific surface area may be due to the expansion of $Ti_3C_2T_x$ interlayer spacing and the inhibition of the stacking degree, which was consistent with the XRD results.

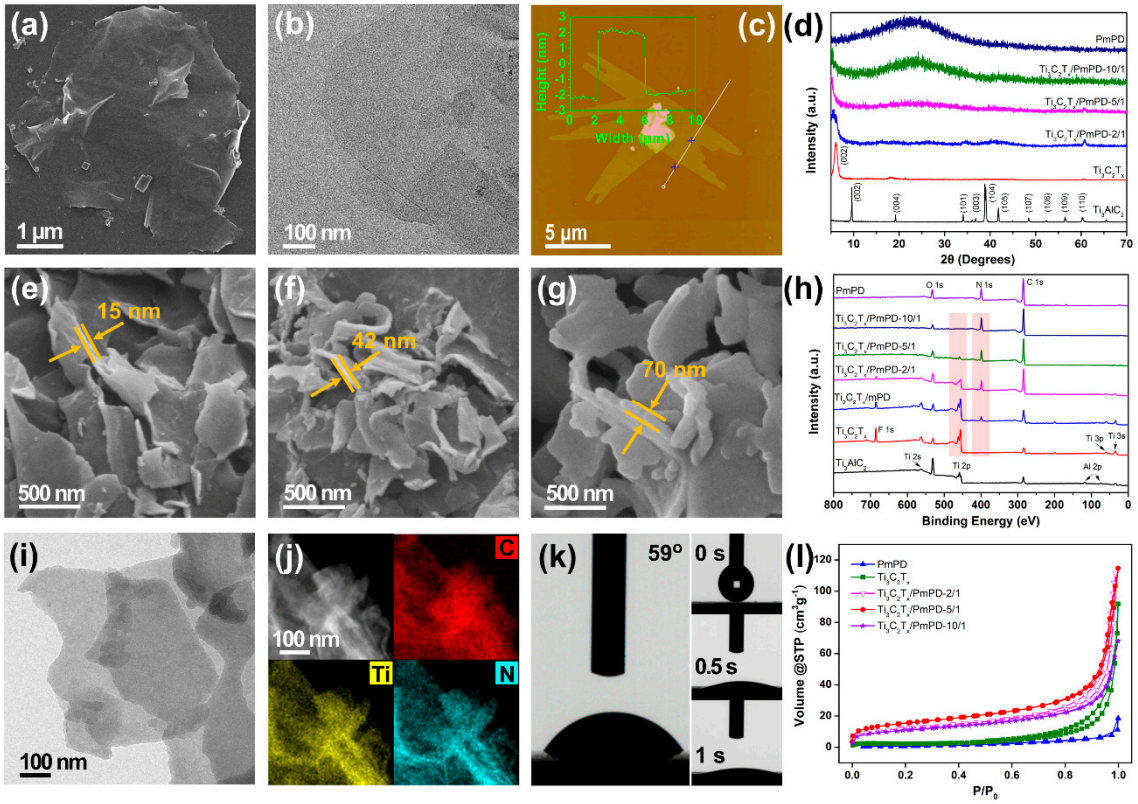

Figure 1. SEM images of (**a**) $Ti_3C_2T_x$, (**e**) $Ti_3C_2T_x$/PmPD-2/1, (**f**) $Ti_3C_2T_x$/PmPD-5/1 and (**g**) $Ti_3C_2T_x$/PmPD-10/1; TEM images of (**b**) $Ti_3C_2T_x$ and (**i**) $Ti_3C_2T_x$/PmPD-5/1; (**c**) AFM image of $Ti_3C_2T_x$; (**d**) XRD patterns of Ti_3AlC_2, $Ti_3C_2T_x$, $Ti_3C_2T_x$/PmPD-X and PmPD; (**h**) XPS survey of Ti_3AlC_2, $Ti_3C_2T_x$, PmPD, $Ti_3C_2T_x$/mPD and $Ti_3C_2T_x$/PmPD-X; (**j**) STEM-EDS mapping of $Ti_3C_2T_x$/PmPD-5/1; (**k**) Water contact angle measurements of $Ti_3C_2T_x$ (right) and $Ti_3C_2T_x$/PmPD-5/1 (left). (**l**) N_2 adsorption−desorption isotherms of $Ti_3C_2T_x$, PmPD and $Ti_3C_2T_x$/PmPD-X.

Table 1. The specific surface area, pore volume, and average pore diameter parameters of Table 2. PmPD and $Ti_3C_2T_x$.

Composites	S_{BET} (m^2 g^{-1})	Pore Volume (cm^{-3} g^{-1})	Average Pore Diameter (nm)
$Ti_3C_2T_x$	10.42	0.14	27.25
$Ti_3C_2T_x$/PmPD-2/1	43.74	0.17	7.86
$Ti_3C_2T_x$/PmPD-5/1	55.93	0.18	6.34
$Ti_3C_2T_x$/PmPD-10/1	38.99	0.11	5.40
PmPD	2.44	0.029	23.54

Raman spectra were recorded to further study the structure characteristics of as-obtained composites. As can be seen from Figure 2a, the modes of $Ti_3C_2T_x$ at 200 and 718 cm^{-1} belonged to the vibrations of Ti and C, respectively. Moreover, the modes at 283, 375, and 618 cm^{-1} belonged to the vibrations of Ti [39]. With the enrichment of mPD, the main peaks of PmPD at 607, 1356 (quinoid imine), and 1567 cm^{-1} (benzenoid amine) appeared on intermediate $Ti_3C_2T_x$/mPD [40]. After in situ polymerization of PmPD, the $Ti_3C_2T_x$ peaks of $Ti_3C_2T_x$/PmPD absolutely disappeared. The Raman spectrogram of $Ti_3C_2T_x$/PmPD had two strong peaks similar to that of PmPD at ~1355 and ~1558 cm^{-1} [41], indicating the strong interaction between PmPD and $Ti_3C_2T_x$.

The chemical composition of $Ti_3C_2T_x$/PmPD were further investigated by XPS technology, and the high-resolution spectra of Ti 2p and C 1s are shown in Figure 2b,c, respectively. Furthermore, the peaks of Ti $2p_{3/2}$ at 455.0, 456.2, 457.5, and 458.8 eV originated from Ti-C, Ti(II), Ti(III), and Ti-O bonds, respectively. The peaks of Ti $2p_{1/2}$ at 461.2, 462.2, 463.0, and 464.3 eV were attributed to Ti-C, Ti(II), Ti(III), and Ti-O bonds, respectively [39,42]. The appearance of Ti(III) revealed that $Ti_3C_2T_x$ was partially oxidized in the process of polymerization. The seven components centered of C 1s core level at 281.8, 282.4, 284.2, 284.8, 285.6, 286.3, and 289.3 eV were attributed to C-Ti, Ti-C-O, C=C, C-C, C-N, C-O, as well as O=C-O bonds, respectively [43,44].

Zeta potentials were recorded to study the surface charge property of $Ti_3C_2T_x$ before and after functionalization. As seen in Figure 2d, $Ti_3C_2T_x$ had a negative surface charge at a wide range of pH because of its terminating functional groups. However, the $Ti_3C_2T_x$/PmPD showed a strongly positive surface charge when the pH value was less than 5. The strongly positive surface probably originated from protonated amino groups (-N^+=) formed by attracting H^+. Therefore, the conversion of $Ti_3C_2T_x$ surface charge from negative to positive verified the successful modification. $Ti_3C_2T_x$/PmPD with positive surface charge would show improved potential in removing anionic Cr(VI).

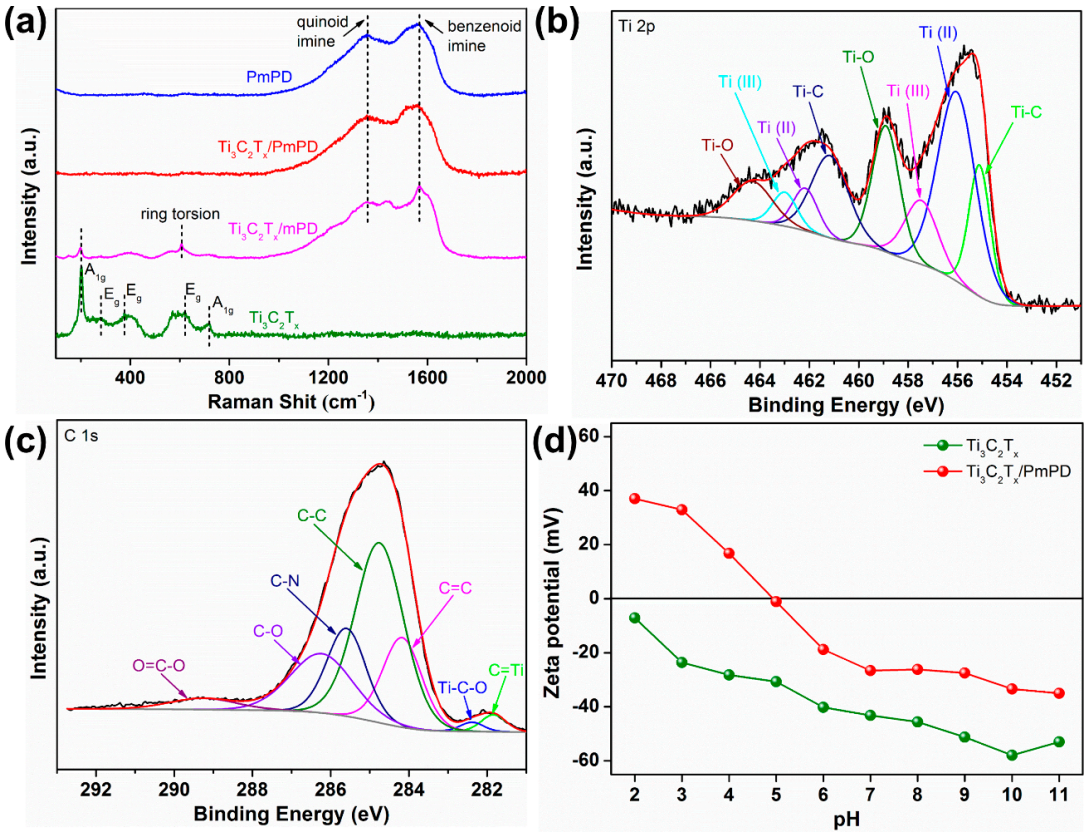

Figure 2. (**a**) Raman spectra of $Ti_3C_2T_x$, PmPD, and $Ti_3C_2T_x$/PmPD. High-resolution spectra of Ti 2p (**b**) and C 1s (**c**). (**d**) Zeta potentials of $Ti_3C_2T_x$/PmPD and $Ti_3C_2T_x$.

The preparation mechanism of $Ti_3C_2T_x$/PmPD is illustrated in Figure 3. Firstly, $Ti_3C_2T_x$ nanosheets were prepared from Ti_3AlC_2 MAX through the MILD method. In the process of functionalization, mPD monomers were attracted to the surface and interlayers of $Ti_3C_2T_x$ nanosheets by electrostatic interaction and hydrogen bonding [37], These interactions induced the formation of intermediate $Ti_3C_2T_x$/PmPD, namely $Ti_3C_2T_x$/mPD. After that, mPD monomers were gradually polymerized on the surface and interlayers of $Ti_3C_2T_x$ when adding oxidant, where $Ti_3C_2T_x$ nanosheets served as templates or substrates. Finally, $Ti_3C_2T_x$/PmPD composite with a positive surface charge and expanded interlayer spacing was obtained.

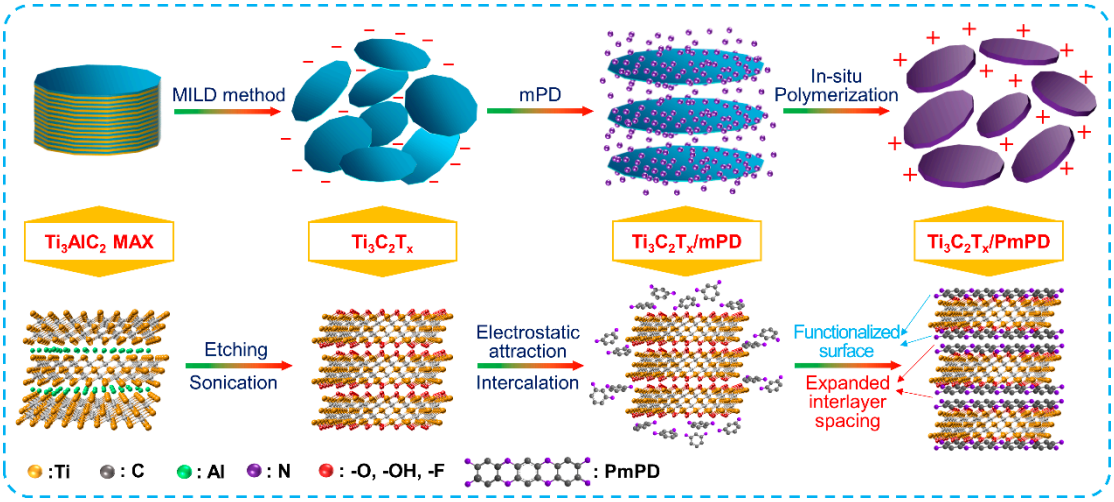

Figure 3. Preparation mechanism of $Ti_3C_2T_x$/PmPD.

3.2. Adsorption Experiments

Adsorption performance of as-obtained composites was firstly investigated, as seen from Figure S2. The adsorption performance of $Ti_3C_2T_x$/PmPD-X was higher than that of PmPD and $Ti_3C_2T_x$. Moreover, $Ti_3C_2T_x$/PmPD-5/1 owned the maximum removal capacity. The remarkable advantage of $Ti_3C_2T_x$/PmPD-X probably originated to the synergistic effects. Therefore, $Ti_3C_2T_x$/PmPD-5/1 was chosen as the representative of $Ti_3C_2T_x$/PmPD in the following experiments.

3.2.1. Effect of pH

The effect of pH on the removal performance of composites was investigated, as shown in Figure 4a. When decreasing pH value, the removal efficiency of Cr(VI) showed an upward trend. pH = 2 was the optimal condition, when Cr(VI) ions mainly existed in the forms of $HCrO_4^-$ (93.03 %) and $Cr_2O_7^{2-}$ (6.42%) (Figure 4a inset) [45]. Low pH facilitated the formation of a strongly positive surface charge, and thus further enhanced the removal capacity of composites. In the next experiments, the optimal pH value was set to 2.

3.2.2. Adsorption Isotherms

The adsorption isotherms were systematically investigated at different initial Cr(VI) concentrations. As seen in Figure 4b, with the increase of initial concentration, the adsorption capacity of PmPD, $Ti_3C_2T_x$ and $Ti_3C_2T_x$/PmPD increased, and finally reached saturation. The isotherms data were fitted by Langmuir, Freundlich, and Redlich–Peterson models to investigate the adsorption process and potential [46,47].

Figure 4b and Table S1 showed the isotherm parameters of the fitting models. The fitting coefficient of Redlich–Peterson model was higher than that of Langmuir and Freundlich model. Therefore, the adsorption behavior of Cr(VI) on $Ti_3C_2T_x$/PmPD was appropriately simulated by the Redlich–Peterson model, indicating the hybrid adsorption process. The maximum theoretical

adsorption capacity of $Ti_3C_2T_x$/PmPD reached 540.47 mg g^{-1}, exceed that of $Ti_3C_2T_x$ (137.45 mg g^{-1}) and pure PmPD (384.73 mg g^{-1}). The excellent adsorption capacity of $Ti_3C_2T_x$/PmPD also overstepped that of the reported MXene-based composites and other typical adsorbents, as can be seen from Table 2, indicating the brilliant application prospects of $Ti_3C_2T_x$/PmPD.

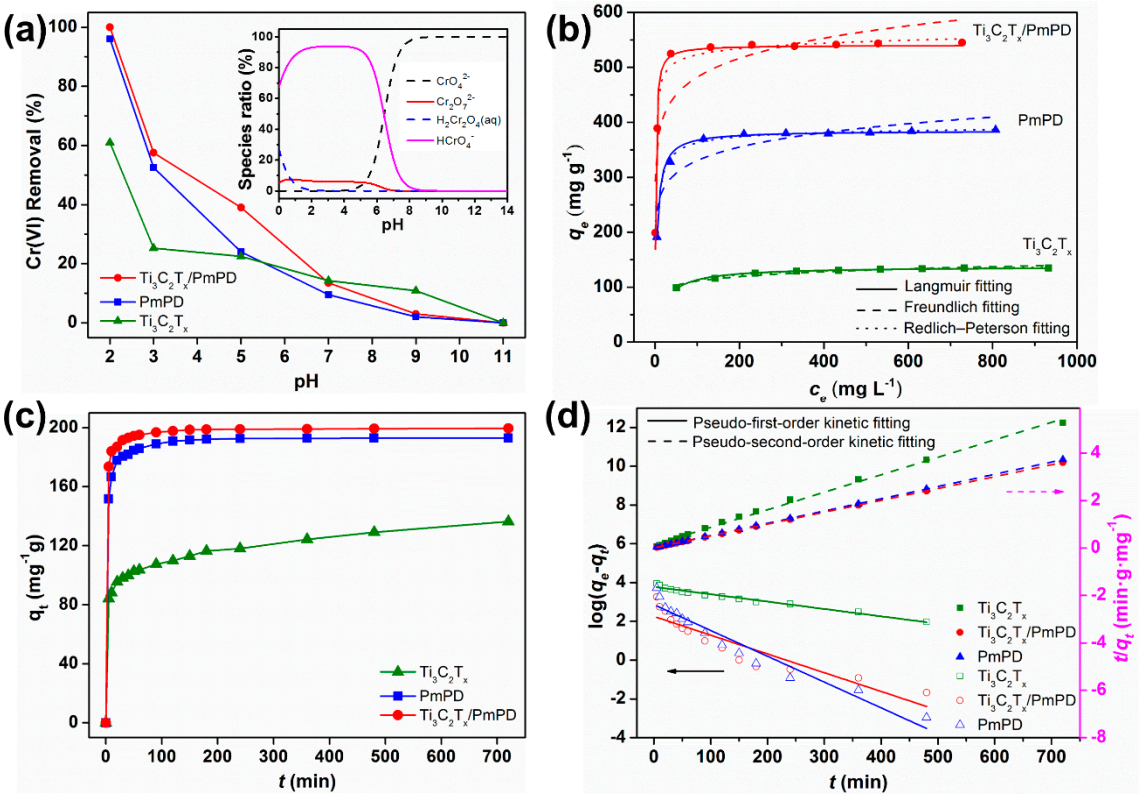

Figure 4. (**a**) Effects of pH (insets, the speciation diagram of Cr(VI) simulated by Visual MINTEQ); (**b**) Isotherms adsorption fitting; (**c**) Effect of adsorption time; (**d**) Pseudo-first-order kinetic model and pseudo-second-order kinetic model fitting.

Table 2. Comparison of removal performance of as-obtained $Ti_3C_2T_x$/PmPD, MXene-based composites, and other typical adsorbents.

Adsorbents	Q_m (mg g^{-1})	pH	References
PDMDAAC	95.2	2	[48]
carbon nano-onions	23.5	3	[49]
Biochar	45.88	2	[50]
Fe@GA beads	33.9	3	[14]
nZVIRS700-Pd	117.1	3	[13]
Modified MXene	225	6	[51]
MXene	250	2	[52]
$Ti_3C_2T_x$/PmPD	540.47	2	this work

3.2.3. Adsorption Kinetics

The effects of contact time on the removal performance of composites were also studied, and the initial Cr(VI) concentration was 100 mg L^{-1}. As seen from Figure 4c, $Ti_3C_2T_x$/PmPD exhibited favorable removal performance than PmPD and $Ti_3C_2T_x$. The removal efficiency of $Ti_3C_2T_x$/PmPD reached 90% within 10 minutes. Moreover, the final removal efficiency was close to 100% within 120 minutes, thereby indicating the excellent adsorption rate. The kinetic data of $Ti_3C_2T_x$/PmPD, PmPD, and $Ti_3C_2T_x$ were fitted by pseudo-first-order and pseudo-second-order adsorption models [50,53]. According to the fitting results (Figure 4d and Table S2), the pseudo-second-order model was suitable

for describing the adsorption process, indicating that the adsorption process was mainly involved chemical adsorption.

3.2.4. Adsorption Mechanism

To better understand the improved removal performance of $Ti_3C_2T_x$/PmPD, the adsorption mechanism was investigated in detail. FT-IR spectra of $Ti_3C_2T_x$/PmPD before and after treating Cr(VI) is shown in Figure 5a. The benzenoid amine peak (~1508 cm^{-1}) of $Ti_3C_2T_x$/PmPD-Cr(VI) was obviously decreased, and the quinoid imine peak (~1620 cm^{-1}) was relatively enhanced, which implied that the oxidation state of $Ti_3C_2T_x$/PmPD was improved after treating Cr(VI) [54].

Furthermore, the chemical compositions of $Ti_3C_2T_x$/PmPD-Cr(VI) and $Ti_3C_2T_x$/PmPD were determined by XPS to further illustrate the adsorption mechanism. As seen from Figure 5b, there were two peaks of Cr2p on $Ti_3C_2T_x$/PmPD-Cr(VI), and the high-resolution spectrum of Cr2p was displayed in Figure 5c. The contributions at ~587.7 and ~577.6 eV originated from Cr(VI), while the contributions at ~586.4 and ~576.6 eV originated from Cr(III) [55]. The appearance of large amounts of Cr(III) (~51.6%) suggested that there was a redox reaction between Cr(VI) and $Ti_3C_2T_x$/PmPD. As seen from Figure 5d, N1s peak of $Ti_3C_2T_x$/PmPD were split into protonated quinoid imine at ~400.49 eV (19.3%), benzenoid amine at ~399.55 eV (62.1%), and quinoid imine at ~398.77 eV (18.6%), respectively [56]. After the treatment of Cr(VI), the percentage of benzenoid amine of $Ti_3C_2T_x$/PmPD-Cr(VI) deceased from 62.1% to 46.9%, and the percentage of the quinoid imine increased from 19.3% to 42.3%. The results implied that there was a conversion of oxidation state from benzenoid amine to quinoid imine resulted from the oxidation of Cr(VI). Moreover, $-N^+=$ also occurred by doping positive Cr(III). It was noted that large percentage of benzenoid amines still existed after the treatment of Cr(VI). Hence, in the next adsorption cycle, Cr (VI) would also be converted into Cr (III) by existing benzenoid amines.

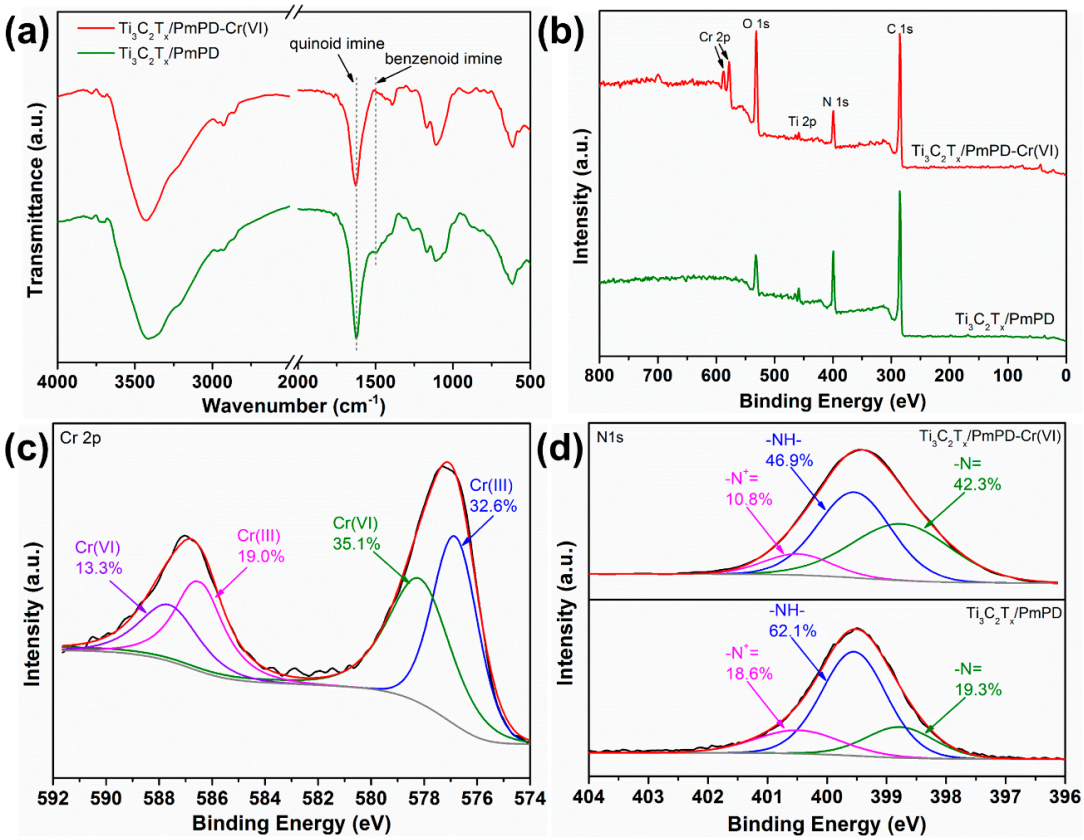

Figure 5. (**a**) FT-IR and (**b**) XPS survey spectra of $Ti_3C_2T_x$/PmPD-Cr(VI) and $Ti_3C_2T_x$/PmPD, respectively. XPS high-resolution of (**c**) Cr2p and (**d**) N1s.

Herein, the adsorption mechanism of $Ti_3C_2T_x$/PmPD could be reasonably deduced, as shown in Figure 6. Firstly, anionic Cr(VI) was adsorbed onto $Ti_3C_2T_x$/PmPD composite. Then, about 51.6% of Cr(VI) were converted to Cr(III) by benzenoid amine. At the same time, benzenoid amine was oxidized to quinoid imine by using Cr(VI). After that, Cr(III) was still adsorbed onto protonated quinoid imine of $Ti_3C_2T_x$/PmPD composite through chelation. Hence, the adsorption process involved adsorption, reduction, and chelation interaction.

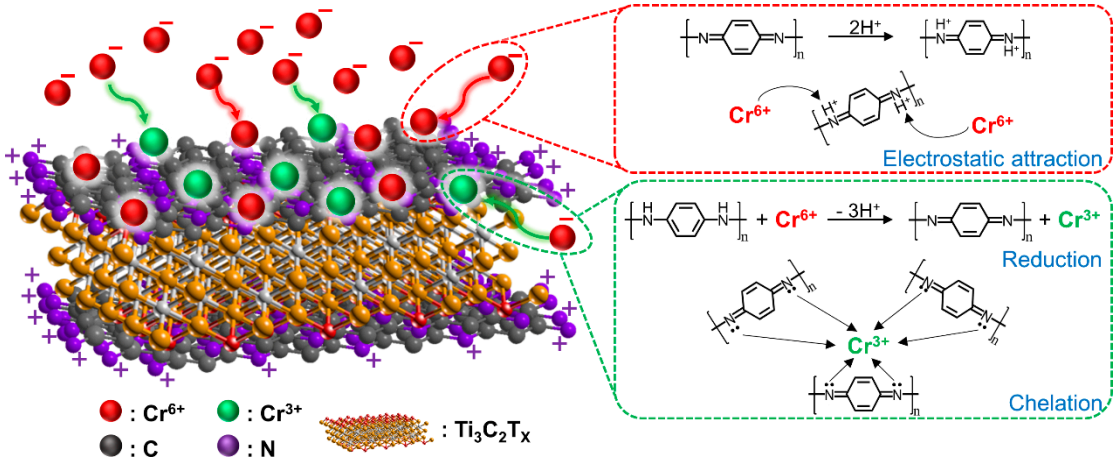

Figure 6. Cr (VI) adsorption mechanism of $Ti_3C_2T_x$/PmPD.

3.2.5. Regeneration

The recycling ability of $Ti_3C_2T_x$/PmPD was evaluated through adsorption-desorption experiments. After adsorption of Cr(VI), $Ti_3C_2T_x$/PmPD was filtrated, rinsed with DI water, and then treated by NaOH solution (0.5 mol L^{-1}) for the next cycle. As seen from Figure 7, the Cr(VI) removal efficiency still remained at ~90% after five recycle rounds with the initial Cr(VI) concentration of 100 ppm, revealing the favorable recycling performance of $Ti_3C_2T_x$/PmPD.

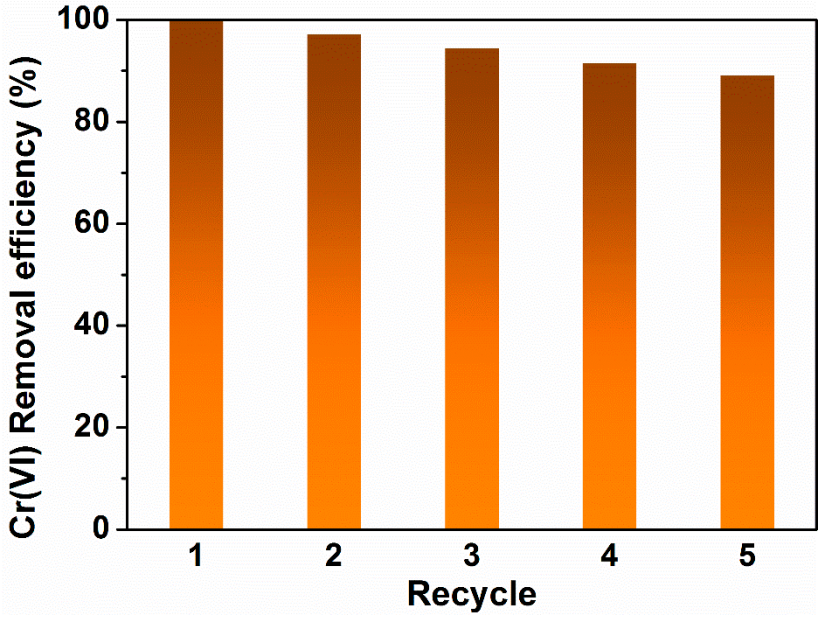

Figure 7. Regeneration of $Ti_3C_2T_x$/PmPD.

4. Conclusions

This research developed a simple strategy to functionalize MXenes for efficient removal of Cr(VI). With the aid of PmPD, the surface charge of $Ti_3C_2T_x$/PmPD was successfully converted from negative to positive. Furthermore, the interlayer spacing of $Ti_3C_2T_x$/PmPD was enlarged from 14.6 to 17.6 Å, and the specific surface area of $Ti_3C_2T_x$/PmPD was increased from 10.42 to 55.93 m^2 g^{-1}. These improvements indicated that the layer-by-layer restacking was successfully restrain. The maximum Cr(VI) adsorption of $Ti_3C_2T_x$/PmPD was 540.47 mg g^{-1}, which was superior to pure PmPD (384.73 mg g^{-1}), $Ti_3C_2T_x$ (137.45 mg g^{-1}), and the reported MXene-based adsorbents. The excellent performance is attributed to the synergistic effects of $Ti_3C_2T_x$ MXene and PmPD. The Cr(VI) adsorption mechanism mainly involved reduction, chelation, and electrostatic interaction. This study indicates that the strategy of in situ polymerization and intercalation was feasible and effective, which provides guidance for enhancing the performance of MXenes in the field of anionic pollutants.

Supplementary Materials: The following are available online at http://www.mdpi.com/1660-4601/17/1/167/s1, Figure S1. SEM and TEM images of PmPD. Figure S2. Adsorption property of $Ti_3C_2T_x$/PmPD-2/1, $Ti_3C_2T_x$/PmPD-5/1, $Ti_3C_2T_x$/PmPD-10/1, $Ti_3C_2T_x$ and PmPD (initial Cr(VI) concentration 500 mg L^{-1} and 1000 mg L^{-1}, pH = 2, temperature 30 °C). Table S1. Parameters of Langmuir, Freundlich and Redlich-Peterson isotherm models of $Ti_3C_2T_x$/PmPD, $Ti_3C_2T_x$, and PmPD. Table S2. Kinetic constants of the pseudo-second-order and pseudo-second order models of Cr(VI) on $Ti_3C_2T_x$/PmPD, $Ti_3C_2T_x$ and PmPD.

Author Contributions: Conceptualization, L.J. and L.C.; Investigation, L.J. and W.Y.; Project administration, L.J. and H.W.; Resources, L.J. and L.Z.; Writing—original draft, L.J.; Writing—review & editing, L.J. All authors have read and agreed to the published version of the manuscript.

Funding: This research is funded by the National Key R&D Program of China (2018YFC1802204), the key project of National Natural Science Foundation of China (51634010), and Key R&D Program of Hunan Province (2018SK2026).

Conflicts of Interest: The authors declare no conflict of interest.

References

1. Lv, D.; Zhou, J.S.; Cao, Z.; Xu, J.; Liu, Y.L.; Li, Y.Z.; Yang, K.L.; Lou, Z.M.; Lou, L.P.; Xu, X.H. Mechanism and influence factors of chromium(VI) removal by sulfide-modified nanoscale zerovalent iron. *Chemosphere* **2019**, *224*, 306–315. [CrossRef] [PubMed]
2. Yan, X.; Song, M.M.; Zhou, M.; Ding, C.L.; Wang, Z.R.; Wang, Y.Y.; Yang, W.C.; Yang, Z.H.; Liao, Q.; Shi, Y. Response of Cupriavidus basilensis B-8 to CuO nanoparticles enhances Cr(VI) reduction. *Sci. Total Environ.* **2019**, *688*, 46–55. [CrossRef] [PubMed]
3. Chai, L.Y.; Ding, C.L.; Li, J.W.; Yang, Z.H.; Shi, Y. Multi-omics response of Pannonibacter phragmitetus BB to hexavalent chromium. *Environ. Pollut.* **2019**, *249*, 63–73. [CrossRef] [PubMed]
4. Estokova, A.; Palascakova, L.; Kanuchova, M. Study on Cr(VI) Leaching from Cement and Cement Composites. *Int. J. Environ. Res. Public. Health* **2018**, *15*, 824. [CrossRef]
5. Serrà, A.; Gómez, E.; Philippe, L. Bioinspired ZnO-Based Solar Photocatalysts for the Efficient Decontamination of Persistent Organic Pollutants and Hexavalent Chromium in Wastewater. *Catalysts* **2019**, *9*, 974. [CrossRef]
6. Geng, J.J.; Yin, Y.W.; Liang, Q.W.; Zhu, Z.J.; Luo, H.J. Polyethyleneimine cross-linked graphene oxide for removing hazardous hexavalent chromium: Adsorption performance and mechanism. *Chem. Eng. J.* **2019**, *361*, 1497–1510. [CrossRef]
7. Park, M.; Park, J.; Kang, J.; Han, Y.S.; Jeong, H.Y. Removal of hexavalent chromium using mackinawite (FeS)-coated sand. *J. Hazard. Mater.* **2018**, *360*, 17–23. [CrossRef]
8. Owlad, M.; Aroua, M.K.; Daud, W.A.W.; Baroutian, S. Removal of Hexavalent Chromium-Contaminated Water and Wastewater: A Review. *Water Air Soil Pollut.* **2008**, *200*, 59–77. [CrossRef]
9. Xiao, R.; Wang, J.J.; Li, R.H.; Park, J.; Meng, Y.; Zhou, B.Y.; Pensky, S.; Zhang, Z.Q. Enhanced sorption of hexavalent chromium [Cr(VI)] from aqueous solutions by diluted sulfuric acid-assisted MgO-coated biochar composite. *Chemosphere* **2018**, *208*, 408–416. [CrossRef]

10. Jiang, D.N.; Huang, D.L.; Lai, C.; Xu, P.; Zeng, G.M.; Wan, J.; Tang, L.; Dong, H.R.; Huang, B.B.; Hu, T.J. Difunctional chitosan-stabilized Fe/Cu bimetallic nanoparticles for removal of hexavalent chromium wastewater. *Sci. Total Environ.* **2018**, *644*, 1181–1189. [CrossRef]
11. El-Mehalmey, W.A.; Ibrahim, A.H.; Abugable, A.A.; Hassan, M.H.; Haikal, R.R.; Karakalos, S.G.; Zakid, O.; Alkordi, M.H. Metal-organic framework@silica as a stationary phase sorbent for rapid and cost-effective removal of hexavalent chromium. *J. Mater. Chem. A* **2018**, *6*, 2742–2751. [CrossRef]
12. Li, L.L.; Feng, X.Q.; Han, R.P.; Zang, S.Q.; Yang, G. Cr(VI) removal via anion exchange on a silver-triazolate MOF. *J. Hazard. Mater.* **2017**, *321*, 622–628. [CrossRef] [PubMed]
13. Qian, L.B.; Liu, S.N.; Zhang, W.Y.; Chen, Y.; Ouyang, D.; Han, L.; Yan, J.C.; Chen, M.F. Enhanced reduction and adsorption of hexavalent chromium by palladium and silicon rich biochar supported nanoscale zero-valent iron. *J. Colloid Interf. Sci.* **2019**, *533*, 428–436. [CrossRef]
14. Zhou, L.L.; Li, R.R.; Zhang, G.L.; Wang, D.F.; Cai, D.Q.; Wu, Z.Y. Zero-valent iron nanoparticles supported by functionalized waste rock wool for efficient removal of hexavalent chromium. *Chem. Eng. J.* **2018**, *339*, 85–96. [CrossRef]
15. Samuel, M.S.; Subramaniyan, V.; Bhattacharya, J.; Chidambaram, R.; Qureshi, T.; Pradeep Singh, N.D. Ultrasonic-assisted synthesis of graphene oxide—Fungal hyphae: An efficient and reclaimable adsorbent for chromium(VI) removal from aqueous solution. *Ultrason. Sonochem.* **2018**, *48*, 412–417. [CrossRef] [PubMed]
16. Zhang, K.X.; Li, H.Y.; Xu, X.J.; Yu, H.W. Synthesis of reduced graphene oxide/NiO nanocomposites for the removal of Cr(VI) from aqueous water by adsorption. *Microporo. Mesopor. Mat.* **2018**, *255*, 7–14. [CrossRef]
17. Vellaichamy, B.; Periakaruppan, P.; Nagulan, B. Reduction of Cr^{6+} from wastewater using a novel in situ-synthesized PANI/MnO_2/TiO_2 nanocomposite: Renewable, selective, stable, and synergistic catalysis. *ACS Sustain. Chem. Eng.* **2017**, *5*, 9313–9324. [CrossRef]
18. Kera, N.H.; Bhaumik, M.; Pillay, K.; Ray, S.S.; Maity, A. Selective removal of toxic Cr(VI) from aqueous solution by adsorption combined with reduction at a magnetic nanocomposite surface. *J. Colloid Interf. Sci.* **2017**, *503*, 214–228. [CrossRef]
19. Naguib, M.; Kurtoglu, M.; Presser, V.; Lu, J.; Niu, J.; Heon, M.; Hultman, L.; Gogotsi, Y.; Barsoum, M.W. Two-dimensional nanocrystals produced by exfoliation of Ti_3AlC_2. *Adv. Mater.* **2011**, *23*, 4248–4253. [CrossRef]
20. Alhabeb, M.; Maleski, K.; Anasori, B.; Lelyukh, P.; Clark, L.; Sin, S.; Gogotsi, Y. Guidelines for synthesis and processing of two-dimensional titanium carbide ($Ti_3C_2T_x$ MXene). *Chem. Mater.* **2017**, *29*, 7633–7644. [CrossRef]
21. Xiong, D.B.; Li, X.F.; Bai, Z.M.; Lu, S.G. Recent advances in layered $Ti_3C_2T_X$ MXene for electrochemical energy storage. *Small* **2018**, *14*, 1703419. [CrossRef] [PubMed]
22. Shahzad, F.; Alhabeb, M.; Hatter, C.B.; Anasori, B.; Hong, S.M.; Koo, C.M.; Gogotsi, Y. Electromagnetic interference shielding with 2D transition metal carbides (MXenes). *Science* **2016**, *353*, 1137–1140. [CrossRef] [PubMed]
23. VahidMohammadi, A.; Moncada, J.; Chen, H.; Kayali, E.; Orangi, J.; Carrero, C.A.; Beidaghi, M. Thick and freestanding MXene/PANI pseudocapacitive electrodes with ultrahigh specific capacitance. *J. Mater. Chem. A* **2018**, *6*, 22123–22133. [CrossRef]
24. Guo, M.; Liu, C.B.; Zhang, Z.Z.; Zhou, J.; Tang, Y.H.; Luo, S.L. Flexible $Ti_3C_2T_X$@Al electrodes with ultrahigh areal capacitance: In situ regulation of interlayer conductivity and spacing. *Adv. Funct. Mater.* **2018**, *28*, 1803196. [CrossRef]
25. Shahzad, A.; Nawaz, M.; Moztahida, M.; Tahir, K.; Kim, J.; Lim, Y.; Kim, B.; Jang, J.; Lee, D.S. Exfoliation of titanium aluminum carbide (211 MAX phase) to form nanofibers and two-dimensional nanosheets and their application in aqueous-phase cadmium sequestration. *ACS Appl. Mater. Interfaces* **2019**, *11*, 19156–19166. [CrossRef]
26. Mu, W.J.; Du, S.Z.; Li, X.L.; Yu, Q.H.; Wei, H.Y.; Yang, Y.C.; Peng, S.M. Removal of radioactive palladium based on novel 2D titanium carbides. *Chem. Eng. J.* **2019**, *358*, 283–290. [CrossRef]
27. Wang, L.; Song, H.; Yuan, L.Y.; Li, Z.; Zhang, Y.J.; Gibson, J.K.; Zheng, L.R.; Chai, Z.F.; Shi, W.Q. Efficient U(VI) reduction and sequestration by Ti_2CT_X MXene. *Environ. Sci. Technol.* **2018**, *52*, 10748–10756. [CrossRef]
28. Wang, L.; Song, H.; Yuan, L.Y.; Li, Z.J.; Zhang, P.; Gibson, J.K.; Zheng, L.; Wang, H.Q.; Chai, Z.F.; Shi, W.Q. Effective removal of anionic Re(VII) by surface-modified Ti_2CT_x MXene nanocomposites: Implications for Tc(VII) sequestration. *Environ. Sci. Technol.* **2019**, *53*, 3739–3747. [CrossRef]

29. Jhon, Y.I.; Koo, J.; Anasori, B.; Seo, M.; Lee, J.H.; Gogotsi, Y.; Jhon, Y.M. Metallic MXene saturable absorber for femtosecond mode-locked lasers. *Adv. Mater.* **2017**, *29*, 1702496. [CrossRef]
30. Xu, Y.X.; Shi, G.Q.; Duan, X.F. Self-assembled three-dimensional graphene macrostructures: Synthesis and applications in supercapacitors. *Acc. Chem. Res.* **2015**, *48*, 1666–1675. [CrossRef]
31. Shen, J.; Liu, G.Z.; Ji, Y.; Liu, Q.; Cheng, L.; Guan, K.; Zhang, M.; Liu, G.; Xiong, J.; Yang, J.; et al. 2D MXene nanofilms with tunable gas transport channels. *Adv. Funct. Mater.* **2018**, *28*, 1801511. [CrossRef]
32. Yu, W.T.; Zhang, L.Y.; Wang, H.Y.; Chai, L.Y. Adsorption of Cr(VI) using synthetic poly(m-phenylenediamine). *J. Hazard. Mater.* **2013**, *260*, 789–795. [CrossRef] [PubMed]
33. Yang, Z.H.; Ren, L.L.; Jin, L.F.; Huang, L.; He, Y.J.; Tang, J.W.; Yang, W.C.; Wang, H.Y. In-situ functionalization of poly(m-phenylenediamine) nanoparticles on bacterial cellulose for chromium removal. *Chem. Eng. J.* **2018**, *344*, 441–452. [CrossRef]
34. Li, X.G.; Huang, M.R.; Duan, W. Novel multifunctional polymers from aromatic diamines by oxidative polymerizations. *Chem. Mater.* **2002**, *102*, 2925–3030. [CrossRef] [PubMed]
35. Zhao, X.; Zha, X.J.; Pu, J.H.; Bai, L.; Bao, R.Y.; Liu, Z.Y.; Yang, M.B.; Yang, W. Macroporous three-dimensional MXene architectures for highly efficient solar steam generation. *J. Mater. Chem. A* **2019**, *7*, 10446–10455. [CrossRef]
36. Li, S.X.; Wang, L.; Peng, J.; Zhai, M.L.; Shi, W.Q. Efficient thorium(IV) removal by two-dimensional Ti_2CT_x MXene from aqueous solution. *Chem. Eng. J.* **2019**, *366*, 192–199. [CrossRef]
37. Boota, M.; Anasori, B.; Voigt, C.; Zhao, M.Q.; Barsoum, M.W.; Gogotsi, Y. Pseudocapacitive electrodes produced by oxidant-free polymerization of pyrrole between the layers of 2D yitanium carbide (MXene). *Adv. Mater.* **2016**, *28*, 1517–1522. [CrossRef]
38. Zhu, Z.Y.; Xie, J.W.; Zhang, M.C.; Zhou, Q.; Liu, F.Q. Insight into the adsorption of PPCPs by porous adsorbents: Effect of the properties of adsorbents and adsorbates. *Environ. Pollut.* **2016**, *214*, 524–531. [CrossRef]
39. Yan, J.; Ren, C.E.; Maleski, K.; Hatter, C.B.; Anasori, B.; Urbankowski, P.; Sarycheva, A.; Gogotsi, Y. Flexible MXene/graphene films for ultrafast supercapacitors with outstanding volumetric capacitance. *Adv. Funct. Mater.* **2017**, *27*, 1701264. [CrossRef]
40. Zhang, C.J.; Pinilla, S.; McEvoy, N.; Cullen, C.P.; Anasori, B.; Long, E.; Park, S.H.; Seral-Ascaso, A.; Shmeliov, A.; Krishnan, D.; et al. Oxidation stability of colloidal two-dimensional titanium carbides (MXenes). *Chem. Mater.* **2017**, *29*, 4848–4856. [CrossRef]
41. Jin, L.F.; Huang, L.; Ren, L.L.; He, Y.J.; Tang, J.W.; Wang, S.; Yang, W.C.; Wang, H.Y.; Chai, L.Y. Preparation of stable and high-efficient poly(*m*-phenylenediamine)/reduced graphene oxide composites for hexavalent chromium removal. *J. Mater. Sci.* **2019**, *54*, 383–395. [CrossRef]
42. Han, F.; Luo, S.J.; Xie, L.Y.; Zhu, J.J.; Wei, W.; Chen, X.; Liu, F.W.; Chen, W.; Zhao, J.L.; Dong, L.; et al. Boosting the yield of MXene 2D sheets via a facile hydrothermal-assisted intercalation. *ACS Appl. Mater. Interfaces* **2019**, *11*, 8443–8452. [CrossRef] [PubMed]
43. Liu, J.; Zhang, H.B.; Sun, R.H.; Liu, Y.F.; Liu, Z.S.; Zhou, A.G.; Yu, Z.Z. Hydrophobic, flexible, and lightweight MXene foams for high-performance electromagnetic-interference shielding. *Adv. Mater.* **2017**, *29*, 1702367. [CrossRef] [PubMed]
44. Wang, H.Y.; He, Y.J.; Chai, L.Y.; Lei, H.; Yang, W.C.; Hou, L.J.; Yuan, T.; Jin, L.F.; Tang, C.J.; Luo, J. Highly-dispersed Fe_2O_3@C electrode materials for Pb^{2+} removal by capacitive deionization. *Carbon* **2019**, *153*, 12–20. [CrossRef]
45. Zhou, B.; Huang, D.Y.; Wu, J.S.; Zhu, Q.H.; Zhu, H.H. Horizontal and Vertical Distributions of Chromium in a Chromate Production District of South Central China. *Int. J. Environ. Res. Public Health* **2018**, *15*, 571. [CrossRef] [PubMed]
46. Gao, Y.; Chen, C.L.; Tan, X.L.; Xu, H.; Zhu, K.R. Polyaniline-modified 3D-flower-like molybdenum disulfide composite for efficient adsorption/photocatalytic reduction of Cr(VI). *J. Colloid Interf. Sci.* **2016**, *476*, 62–70. [CrossRef]
47. Wang, T.; Zhang, L.Y.; Li, C.F.; Yang, W.C.; Song, T.T.; Tang, C.J.; Meng, Y.; Dai, S.; Wang, H.Y.; Chai, L.Y.; et al. Synthesis of core-shell magnetic Fe_3O_4@poly(m-Phenylenediamine) particles for chromium reduction and adsorption. *Environ. Sci. Technol.* **2015**, *49*, 5654–5662. [CrossRef]

48. Li, N.; Yue, Q.Y.; Gao, B.Y.; Xu, X.; Kan, Y.J.; Zhao, P. Magnetic graphene oxide functionalized by poly dimethyl diallyl ammonium chloride for efficient removal of Cr(VI). *J. Taiwan Inst. Chem. E* **2018**, *91*, 499–506. [CrossRef]
49. Sakulthaew, C.; Chokejaroenrat, C.; Poapolathep, A.; Satapanajaru, T.; Poapolathep, S. Hexavalent chromium adsorption from aqueous solution using carbon nano-onions (CNOs). *Chemosphere* **2017**, *184*, 1168–1174. [CrossRef]
50. Zhang, X.J.; Zhang, L.; Li, A.M. Eucalyptus sawdust derived biochar generated by combining the hydrothermal carbonization and low concentration KOH modification for hexavalent chromium removal. *J. Environ. Manag.* **2018**, *206*, 989–998. [CrossRef]
51. Zou, G.D.; Guo, J.X.; Peng, Q.M.; Zhou, A.G.; Zhang, Q.R.; Liu, B.Z. Synthesis of urchin-like rutile titania carbon nanocomposites by iron-facilitated phase transformation of MXene for environmental remediation. *J. Mater. Chem. A* **2016**, *4*, 489–499. [CrossRef]
52. Ying, Y.L.; Liu, Y.; Wang, X.Y.; Mao, Y.Y.; Cao, W.; Hu, P.; Peng, X.S. Two-dimensional titanium carbide for efficiently reductive removal of highly toxic chromium(VI) from water. *ACS Appl. Mater. Interfaces* **2015**, *7*, 1795–1803. [CrossRef] [PubMed]
53. Cai, W.Q.; Gu, M.M.; Jin, W.; Zhou, J.B. CTAB-functionalized C@SiO_2 double-shelled hollow microspheres with enhanced and selective adsorption performance for Cr(VI). *J. Alloy Compd.* **2019**, *777*, 1304–1312. [CrossRef]
54. Li, X.G.; Ma, X.L.; Sun, J.; Huang, M.R. Powerful reactive sorption of silver(I) and mercury(II) onto poly(o-phenylenediamine) microparticles. *Langmuir* **2009**, *25*, 1675–1684. [CrossRef] [PubMed]
55. Jin, L.F.; Chai, L.Y.; Ren, L.L.; Jiang, Y.X.; Yang, W.C.; Wang, S.; Liao, Q.; Wang, H.Y.; Zhang, L.Y. Enhanced adsorption-coupled reduction of hexavalent chromium by 2D poly(m-phenylenediamine)-functionalized reduction graphene oxide. *Environ. Sci. Pollut. Res.* **2019**, *26*, 31099–31110. [CrossRef] [PubMed]
56. Zhang, L.Y.; Wang, Y.Y.; Peng, B.; Yu, W.T.; Wang, H.Y.; Wang, T.; Deng, B.W.; Chai, L.Y.; Zhang, K.; Wang, J.X. Preparation of a macroscopic, robust carbon-fiber monolith from filamentous fungi and its application in Li–S batteries. *Green Chem.* **2014**, *16*, 3926. [CrossRef]